

See discussions, stats, and author profiles for this publication at: <https://www.researchgate.net/publication/257420342>

Role of Adsorbing Moieties on Thermal Conductivity and Associated Properties of Nanofluids

ARTICLE *in* THE JOURNAL OF PHYSICAL CHEMISTRY C · MAY 2013

Impact Factor: 4.77 · DOI: 10.1021/jp401792b

CITATIONS

13

READS

99

2 AUTHORS:



Anbumozhi Angayarkanni

Indira Gandhi Centre for Atomic Research

12 PUBLICATIONS 66 CITATIONS

SEE PROFILE



John Philip

Indira Gandhi Centre for Atomic Research

179 PUBLICATIONS 3,176 CITATIONS

SEE PROFILE

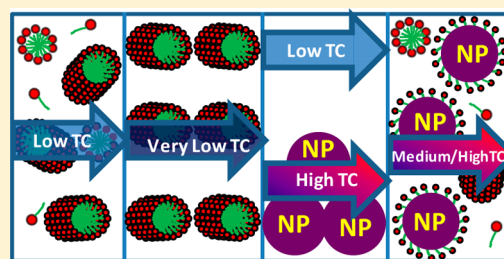
Role of Adsorbing Moieties on Thermal Conductivity and Associated Properties of Nanofluids

S. A. Angayarkanni and John Philip*

SMARTS, Metallurgy and Materials Group, Indira Gandhi Centre for Atomic Research, Kalpakkam-603 102, India

ABSTRACT: We probe the contributions of adsorbing moieties (surface active species) on thermal conductivity (k), rheology, density, contact angle, and refractive index of nanofluids. The role of surface morphology, initial thermal conductivity of solid particles and their number density on thermal property enhancement of nanofluids is also studied. Our studies on a model soft sphere system, consisting of micelles of an average size of 2.5–7 nm with different headgroup charges, show that the thermal conductivity of ionic surfactant micelles follows the effective medium theory of poor thermal conductors, i.e., $1 - 3\phi/2$ with the interfacial resistance tending to infinity, where ϕ is the volume fraction. The results suggest that the long alkyl chain group of nonionic surfactant micelles are poor thermal conductors at very low concentrations with large interfacial

tension compared to their anionic counterparts. The k measurement in aqueous alumina, silica, and nonaqueous iron oxide nanofluids with particle size in the range of 12–15 nm shows that the presence of excess surfactant does not lower the thermal conductivity enhancement in nanofluids, though the latter has a much lower thermal conductivity than the base fluid. The adsorbed moieties indeed enhance the stability of nanoparticles in the base fluids. Further, our studies show that the k enhancement in nanofluids is independent of the initial thermal properties of suspended particles. For both “soft” and “hard” sphere particles, the k follows the effective medium theory for poor and good conductors, respectively. Further, our results show that the orientation of cylinders and their aspect ratio are key to the thermal conductivity enhancement in nanofluids. While cylinders with higher aspect ratio and random ordering give a lower k , orientated cylinders with higher aspect ratio provide dramatic enhancement in the k . These findings are very useful for engineering efficient nanofluids for thermal managements.



1. INTRODUCTION

Thermal properties of materials are extremely important for heat transfer applications.^{1,2} The quest for efficient cooling materials led to the emergence of a new field of research called nanofluids.^{3–19} Any nanomaterials such as nanoparticles, nanotubes, and nanosheets suspended in carrier fluids are called nanofluids. Nanofluids and nanomaterials have been a topic of great interest during the past decade primarily due to the initial reports of anomalous thermal conductivity enhancement (i.e., beyond Maxwell's limits) in nanofluids with a small percentage of nanoparticles.³ Several recent studies in stable nanofluids show enhancement within Maxwell's limits.^{7,20–22} The reasons for the reported anomalous enhancement in thermal conductivity in nanofluids are still a topic of debate.^{20,23} After considering various mechanisms responsible for the observed enhancement in k , one of the most probable aspects considered in recent years is the effective conduction of heat through percolating aggregating nanoparticle paths.^{18,24,25} However, many researchers still believe that micronanoconvection could be another plausible cause for thermal conductivity enhancement.^{26,27} Another gray area in the understanding of thermal property variations in nanofluids is the role of interfacial resistance (γ)^{2,28} and the morphology of suspended nanoparticles in fluids. The former aspect is extremely important because most of the suspensions are stabilized using a surface active species or surfactant. Though the mechanism of stabilization of nanoparticles by surfactants is

quite well understood, their precise role in interfacial thermal resistance (Kapitza resistance, R_b) and in thermal and rheological properties of nanofluids is still unclear.^{15,29–35} Therefore, a systematic study to understand the effect of interfacial resistance on thermal conductivity of liquids and suspensions is warranted, which is one of the key issues addressed in this paper.

Nanofluids are thermodynamically unstable systems. However, they can be made kinetically stable with the aid of suitable surface active species. Unlike molecular fluids, production of well-stabilized nanofluids is a difficult task. For production of stable nanofluids, one has to first produce fairly monodisperse nanoparticles and then functionalize them with a stabilizing moiety to prevent interparticle attractions. Owing to the large surface area to volume ratio of fine nanomaterials, the dispersed particles (even with stabilizing entities) have a tendency to aggregate through van der Waals attraction. Even with the best available production route, it is difficult to produce nanoparticles with polydispersity less than 5%. However, to unravel the exact mechanism of heat conduction in nanofluids, model systems with a high degree of monodispersity and well controlled morphology are necessary. To resolve the problem of high polydispersity of nanoparticles, we choose model

Received: February 20, 2013

Revised: April 5, 2013

Published: April 5, 2013

systems of micellar fluids with remarkable monodispersity, along with typical nanofluids, for our studies.

Though there are several studies on the viscosity (η) of nanofluids, a proper understanding of the role of η on k enhancement is still missing, which is a very important aspect for thermal engineering. The particle concentration, particle–particle interactions, agglomeration, and clustering of suspended entities play major roles in the effective viscosity (η/η_0), where η_0 is the viscosity of base fluid.³⁶ The rheological properties of nanofluids are strongly related to the conformation of suspended particles in base fluids. Agglomeration in nanofluids is an undesirable effect that is difficult to control. Since the agglomeration issue is practically negligible in micellar systems due to electrostatic or steric stabilization, it is one of the best model systems to study the role of viscosity on thermal and related properties.

The questions that we address in this study are the following: (a) Does the k enhancement in “soft” and “hard” nanofluids follow effective medium theory (EMT)? (b) What is the role of the initial thermal conductivity, morphology, and number density (ND) of suspended particles on thermal conductivity enhancement? (c) Do surface active moieties at nanoparticle interfaces enhance or reduce the k of nanofluids? (d) What is the role of the aspect ratio of a particle and its orientation with respect to heat flow direction on the k enhancement? For these studies, we prepare model soft systems of micelles in the size range of 2.5–7 nm with different headgroup charges and water-based alumina and silica nanofluids and a nonaqueous, kerosene-based iron oxide nanofluid with particle size in the range of 12–15 nm. Through these systematic studies, we not only shed light on to the effect of surface active species on thermal conductivity, rheology, density, contact angle (θ), and refractive index but also provide best practices to tailor nanofluids suitable for effective heat transfer applications.

2. MATERIALS AND METHODS

2.1. Materials. An anionic surfactant, sodium dodecyl sulfate ($\text{C}_{12}\text{H}_{25}\text{SO}_4\text{Na}$, hereafter referred to as SDS); cationic surfactant, cetyltrimethylammonium bromide (CTAB); and nonionic surfactants, nonylphenol ethoxylate (NP9 and NP10), were purchased from Sigma. All chemicals were used without further purification. The critical micellar concentrations (cmc) for SDS, CTAB, NP9, and NP10 are 8×10^{-3} , 9×10^{-4} , 6×10^{-5} , and 7×10^{-5} M, respectively. The reported micellar diameter of SDS, CTAB, NP9, and NP10 are approximately 3.7, 5.0, 6.3, and 6.8 nm, respectively.^{37–40} The average aggregation number of micelles of SDS, CTAB, NP9, and NP10 are 64, 95, 350, and 144, respectively.^{37,41–43} For our studies, 16 vol % stock solutions of SDS, CTAB, NP9, and NP10 surfactants were prepared using Milli-Q water with a resistivity value of 18.2 M Ω cm from which different concentrations were prepared. The structures of these four surfactants are shown in Figure 1.

Water-based aluminum oxide (Al_2O_3) and silicon dioxide (SiO_2) nanofluids and oil-based iron oxide (Fe_3O_4) nanofluid are used to study the effect of adsorbed surfactant layer on thermal conductivity. The water-based Al_2O_3 nanofluid was purchased from Numex Private Ltd, and aqueous SiO_2 nanofluid was purchased from Chempure Private Ltd. The Fe_3O_4 nanofluid was prepared in our laboratory. All these suspensions were stable against gravitational settling. Magnetite nanoparticles were prepared by the chemical coprecipitation technique.⁴⁴ The details are briefly discussed. The freshly

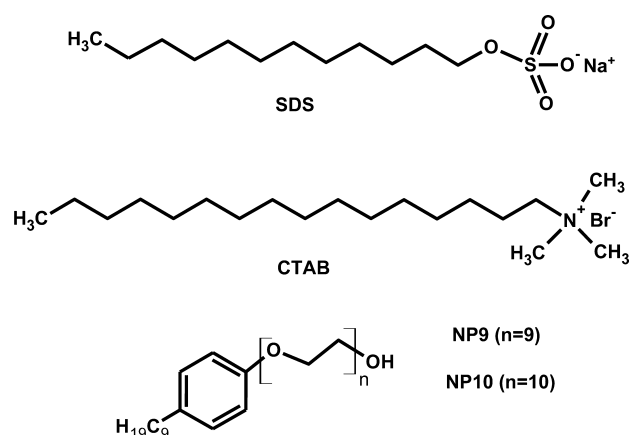


Figure 1. The structure of SDS, CTAB, NP9, and NP10 surfactants.

prepared iron salt solutions of 0.2 M $\text{FeCl}_2 \cdot 4\text{H}_2\text{O}$ and 0.4 M $\text{FeCl}_3 \cdot 6\text{H}_2\text{O}$ were mixed at a 1:1 ratio at a constant stirring speed of 1000 rpm. After the addition of ammonia solution, the pH of the solution reached a value of 10. When the solution turned black, 20 mL of oleic acid was added and the dispersion pH was adjusted to 9.5. Then the temperature was increased to 70 °C. The solution was kept at the same pH, temperature, and stirring speed for 30 min to finish the coating process. After this step, the temperature was increased to 79 °C in order to eliminate the excess ammonia and to protonate the adsorbed and unadsorbed ammonium oleate as oleic acid. The surfactant coated particles were washed with triply distilled water at 60 °C, to remove the ionic impurities, and later the particles were dispersed in hexane. The hexane dispersion was treated with acetone to induce aggregation of particles. The aggregated particles were then separated from dispersion by centrifugation at 2500 rpm for 30 min. The precipitated magnetite nanoparticles were again dispersed in hexane for further treatment. The hexane/acetone mixture washing procedure was repeated again to remove excess surfactant in the dispersion. The surfactant-coated magnetite nanoparticles were dried at 35 °C for 48 h in inert atmosphere, and then the dried particles were dispersed in kerosene.

2.2. Methods. The thermal conductivity of the samples was measured by using a hot wire probe as per the procedure discussed earlier.⁴⁴ All the k measurements have been carried out at 25 °C. The probe was standardized first by measuring the thermal conductivity of three standard liquids, water, ethylene glycol, and kerosene; the measured values were in good agreement with literature values. Further, the k measurements in these three samples was also determined using a hot disk thermal constants analyzer (TPS 2500s) for comparison. The results obtained from both the techniques were similar, except for a minor prefactor correction.

Viscosity measurements were carried out using a strain-controlled rheometer from Anton Paar (MCR 301) in cone and plate geometry with a Peltier temperature controller system. A DMA 35 portable densitometer (Anton Paar) was used for density measurements. Contact angle measurements were carried out using a Holmarc (Kochi) contact angle measuring instrument. Three microliters of each sample was filled in a sterile syringe and was dropped on the stainless steel substrate. The drop image was obtained using U Eye demo software. The contact angles were then measured using image analysis software. Ten readings were obtained for each sample, and the average was taken.

Refractive index measurements were done using a digital refractometer with a Peltier-based temperature controller (Rudolph). Small angle X-ray scattering (SAXS) studies for nanofluids were carried out using a Rigaku Ultima IV instrument. It uses Cu K α ($\lambda = 1.5418$ Å) as X-ray source. The scattering intensity $I(q)$ was measured as a function of the scattering vector [$q = (4\pi \sin \theta)/\lambda$]. The scattering intensity plot was fitted with the spherical model equation $I(q) = |\Delta\rho|^2 \{ (4\pi/q^3) [\sin(qD/2) - (qD/2)\cos(qD/2)] \}^2$, where D is the diameter of the particle and $\Delta\rho$ is the difference in electron density of the particle and the suspended medium. The most probable particle size was obtained from the distance distribution function. Fourier-transform infrared spectroscopy (FTIR) studies were done using ABB Bomem MB 3000 instrument. For FTIR studies, the dried samples were mixed thoroughly with powdered KBr and pressed to form a transparent pellet. The spectrum was obtained in the wavelength range of 400–3600 cm^{-1} . The thermogravimetric analysis (TGA) of nanofluids was carried out using a Mettler Toledo TGA/DSC system under inert atmosphere from 30 to 600 °C at a heating rate of 5 °C/min.

3. RESULT AND DISCUSSION

3.1. DLS, SAXS, FTIR, and TGA Analysis. Figure 2 shows the hydrodynamic diameter of the water- and kerosene-based

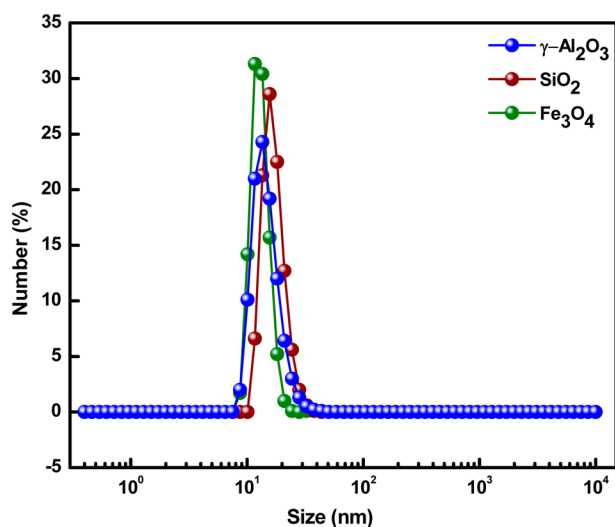


Figure 2. Hydrodynamic size distribution obtained from dynamic light scattering measurement for water-based, uncoated $\gamma\text{-Al}_2\text{O}_3$ and SiO_2 nanofluids and oleic acid-coated kerosene-based Fe_3O_4 nanofluid.

nanofluids. The average hydrodynamic sizes are found to be 13, 15, and 12.5 nm for $\gamma\text{-Al}_2\text{O}_3$, SiO_2 , and Fe_3O_4 nanoparticles, respectively. The size distribution is found to be narrow for all the three nanofluids. Figure 3a shows the X-ray scattering intensity as a function of scattering vector, and Figure 3b shows the particle size distribution obtained from the best fit on SAXS data for water-based Al_2O_3 and SiO_2 nanofluids and kerosene-based Fe_3O_4 nanofluid. The most probable particle size is found to be 10.74 nm for Al_2O_3 nanoparticle, 14.7 nm for SiO_2 nanoparticle, and 11.66 nm for Fe_3O_4 nanoparticle. The average hydrodynamic diameter measured by DLS was slightly higher than that obtained from the SAXS results. The thermogravimetric curves for $\gamma\text{-Al}_2\text{O}_3$ and SiO_2 nanofluids and Fe_3O_4 nanoparticle are shown in Figure 4. The

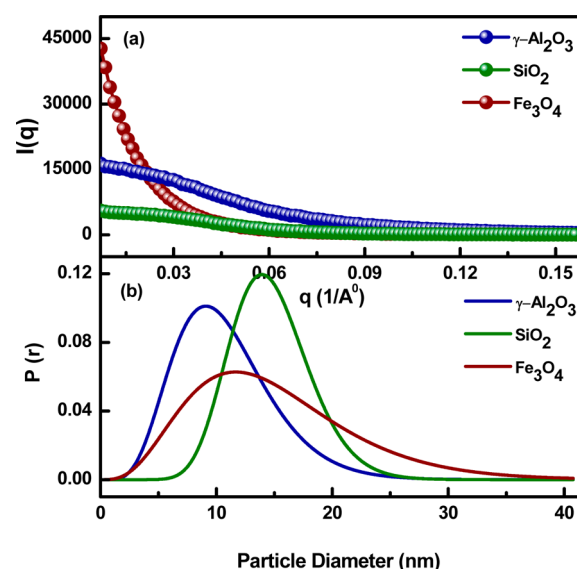


Figure 3. (a) The small-angle X-ray scattering intensity as a function of scattering vector and (b) the particle size distribution obtained from the best fit on SAXS data for water-based $\gamma\text{-Al}_2\text{O}_3$ and SiO_2 nanofluids and kerosene-based Fe_3O_4 nanofluid.

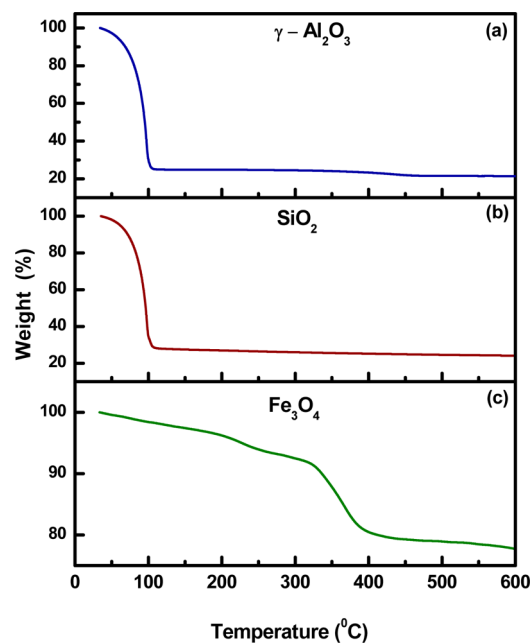


Figure 4. The thermogravimetric curves for water-based (a) $\gamma\text{-Al}_2\text{O}_3$ and (b) SiO_2 nanofluids and (c) oleic acid-coated Fe_3O_4 nanoparticle.

thermogravimetric curves for water-based $\gamma\text{-Al}_2\text{O}_3$ and SiO_2 nanofluids (Figure 4a,b) show a single-step weight loss at ≈ 103 °C (~ 75 wt %) and ≈ 105 °C (~ 71 wt %), respectively, corresponding to the loss of most of the water. Thereafter, a gradual decrease in weight is observed till 600 °C in both the cases. The gradual decrease in weight observed beyond 100 °C (till 600 °C) was about ~ 4 and 6 wt %, respectively for $\gamma\text{-Al}_2\text{O}_3$ and SiO_2 nanofluids. The decrease in weight observed beyond 100 °C in the cases of $\gamma\text{-Al}_2\text{O}_3$ may be due to the dehydroxylation of the alumina surface.⁴⁵ The weight loss observed in $\gamma\text{-Al}_2\text{O}_3$ in the temperature range of 100–600 °C was similar to that observed by Costa et al.⁴⁵ A similar trend in the thermogram was also observed in SiO_2 nanofluid. The TGA

curve for the magnetite nanoparticles shows a two-step weight loss between 199 and 310 °C (~4 wt %) and between 310 and 400 °C (~12 wt %) (Figure 4c). The first step should be due to the removal of loosely bound or free surfactant, and the second step should be due to the removal of strongly bound surfactant molecules. The FTIR spectra for Al_2O_3 , SiO_2 , and Fe_3O_4 nanofluids are shown in Figure 5. Figure 5a corresponds to

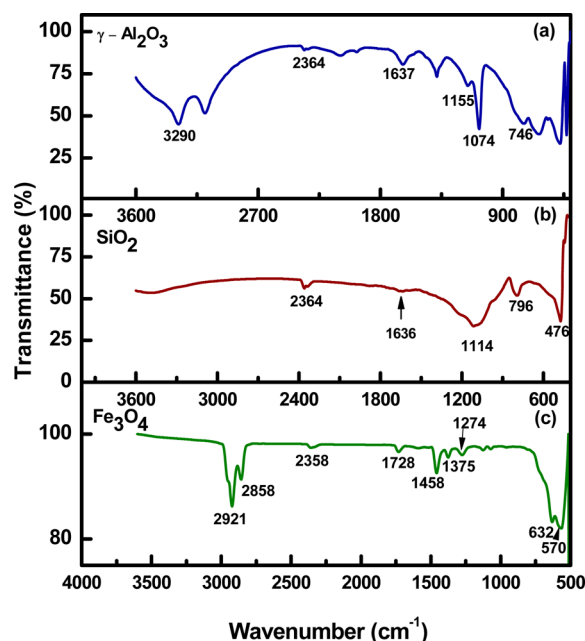


Figure 5. FTIR spectra of (a) $\gamma\text{-Al}_2\text{O}_3$, (b) SiO_2 , and (c) oleic acid-coated Fe_3O_4 .

to the FTIR spectrum of water-based $\gamma\text{-Al}_2\text{O}_3$ nanofluid. The transmittance band at 746 cm^{-1} corresponds to the stretching vibration of Al–O. The spectrum shows characteristic peaks at 1074 and 1155 cm^{-1} , which correspond to the Al–O–Al symmetric bending and stretching vibrations and Al–O–Al asymmetric bending modes, respectively. The transmittance band at 1637 and 3290 (3575 cm^{-1}) corresponds to bending⁴⁵ and stretching modes of water, respectively. Figure 5b corresponds to FTIR spectrum of SiO_2 nanofluid. The rocking and symmetric and asymmetric stretching of Si–O–Si are observed at 476 , 796 , and 1114 cm^{-1} , respectively. The FTIR spectrum of oleic acid-coated iron oxide nanoparticles dispersed in kerosene is shown in Figure 5c. The spectrum shows characteristic peaks at 2921 , 2858 , 2358 , 1728 , 1458 , 1375 , 1274 , 632 , and 570 cm^{-1} . The symmetric and asymmetric stretching mode of the methylene group of the oleic acid appears at 2858 and 2921 cm^{-1} , respectively. The peak at 1458 cm^{-1} corresponds to the asymmetric stretching of the carboxylate (COO^-) group. The peak at 570 cm^{-1} is attributed to the stretching of bonds between octahedral and tetrahedral metal ions to oxide ions, while the one at 1728 cm^{-1} is due to the presence of free oleic acid molecules. The rest of the peaks are attributed to the vibrations in kerosene. In all the three cases, a peak is noticed around 2360 cm^{-1} that corresponds to the asymmetric stretching mode of carbon dioxide.

3.2. Effect of Number Density of Dispersed Particle on Thermal Conductivity. Figure 6 shows the variation of effective thermal conductivity (k/k_f) and the percentage (%) of decrease in thermal conductivity (k) as a function of surfactant concentration for SDS, CTAB, NP9, and NP10 in water. Here,

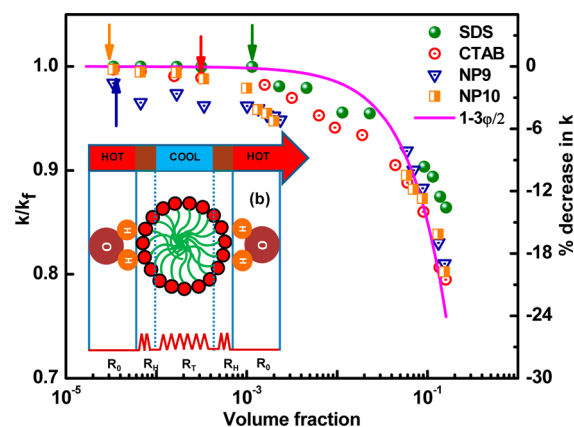


Figure 6. The variation of thermal conductivity as a function of volume fraction for SDS, CTAB, NP9, and NP10 along with the theoretical fit (The cmc values of surfactants are shown by arrows of respective symbol colors). The inset in the figure shows the schematic representation of micelles and the possible thermal resistive contributions from different moieties (headgroup, tail, and water molecules). The maximum interfacial resistance is offered by the hydrophobic tail part and the minimum by the fluid molecules. R_b , R_t , R_f represents the resistance offered by water molecules, headgroup, and tail, respectively.

k and k_f are the thermal conductivities of the nanofluid and water, respectively. It should be noted that the surfactants are amphiphilic molecules with hydrophilic and hydrophobic parts. The surfactant molecules exist as unimers at concentrations below the cmc and form spherical micelles above the cmc. The driving forces for micelle formation are the hydrophobic force and entropy. The forces opposing micelle formation are concentration gradient, thermal motion, and electrostatic repulsion between ionic polar heads (applicable to CTAB and SDS only). In all the four systems, the k/k_f is found to decrease with increase in surfactant concentration. The micellar system is a disordered system. As the surfactant concentration increases, the number of micelles in the system increases, leading to an increase in the degree of disorder, which has resulted in a decrease in k/k_f with an increase in surfactant concentration. Similar results were reported by Andersen,⁴⁶ who observed that an increase in the disorder of the system can decrease the thermal conductivity. Muller⁴⁷ has suggested that the strength of the interatomic binding force is related to thermal conductivity. The greater the strength of this binding force, the higher the thermal conductivity. The higher interatomic binding force in metals results in higher thermal conductivity. The binding force is weak in the case of micellar systems due to its disordered structures leading to a lower thermal conductivity. The number density for the micellar system is given by $\text{ND} = (6\phi)/(\pi d^3)$, where ϕ is the volume fraction of the particle and d is the diameter of the particle. According to Maxwell theory,⁴⁸ for a dilute suspension of spherical particles, the $k/k_f = (1 + 2\beta\phi)/(1 - 2\beta\phi)$ where $\beta = (k_p - k_f)/(k_p + 2k_f)$ and k_p and k_f are the thermal conductivities of the nanoparticles (dispersed phase of micelles in the present case) and base fluid, respectively. To account for the interfacial thermal resistance (R_b), k_f is modified as $k_f \rightarrow k_f + \alpha k_p$, where $\alpha = (R_b k_f)/d$ and d is the average micellar size. In a nanofluid, series and parallel modes of thermal conduction through the base fluid and the nanoparticles can be visualized within the mean-field models. The parallel mode has the geometric configuration that allows the most efficient mode of heat

propagation.⁷ Hashin and Shtrikman (HS) bounds for thermal conductivity of a nanofluid, on the basis of volume fraction alone, is given by⁴⁹

$$k_f \left[1 + \frac{3\varphi[k]}{3k_f + (1 - \varphi)\kappa} \right] \leq k \leq \left[1 - \frac{3(1 - \varphi)[k]}{3k_p - \varphi[k]} \right] k_p \quad (1)$$

In the lower HS limit, nanoparticles are well-suspended and conduction is through series mode, whereas in the upper HS limit, the conduction path is through dispersed particles. In the limit $\varphi k_p/k_f \gg 1$, the predicted values of k/k_f for the upper HS and parallel modes are $(2\varphi/3)k_p/k_f$ and $\varphi k_p/k_f$, respectively. The upper and lower bounds reverse in our case, as $k_p < k_f$. The EMT fits are shown by the solid line in Figure 6. It can be seen that the experimental data show large deviation from effective medium theory at low volume fractions of micelles, especially for CTAB and NP9. At lower volume fraction, the number of micelles in the system is less, and therefore, the interfacial thermal resistance is also less. As the volume fraction increases, the number of micelles in the system increases, which leads to higher interfacial thermal resistance. The lower interfacial thermal resistance at lower concentration might be the probable reason for the observed large deviation from theoretical fit at lower volume fractions. For volume fractions above 0.06, the experimental data fit quite well with the effective medium theory.

In general, the interfacial thermal resistance reduces the effective thermal conductivity. When $\alpha \rightarrow \infty$, k/k_f reduces to $1 - 3\varphi/2$, where the effective thermal conductivity becomes smaller than that of the base fluid. A negative interfacial thermal (Kapitza) resistance means an interfacial thermal gradient that is lower than that of the bulk region. A positive R_b leads to a decrease in the effective thermal conductivity. Simulation studies in nanofluids showed that a positive Kapitza length, due to a weak solid–fluid interaction, can lead to a negligible or negative thermal conductivity enhancement.^{50,51} The non-equilibrium molecular dynamics simulations show that the thermal conductivity of a well-dispersed nanofluid can be enhanced beyond the Maxwell limit through a percolating amorphous-like fluid structure at the cluster interface, due to strong cluster–fluid interaction.⁵² Our experimental data suggest that the interfacial resistance in the presence of surfactant is positive but far from infinity. The interfacial thickness given by Yan⁵³ is $h = (1/\sqrt{3})[(4M_f)/(\rho_f N_a)]^{1/3}$, where M_f and ρ_f are the molecular weight and density of the surrounding fluid medium around a nanocluster, and N_a is Avogadro's number. Using the above equation, the calculated value of interfacial thickness for water, SDS, CTAB, NP9, and NP10 are found to be 2.84, 71.5, 77, 90.9, and 93.7 nm, respectively. The observed larger reduction of k , especially at lower surfactant concentrations in NP9 and NP10, followed by CTAB and SDS, are consistent with the theoretical values of interfacial thickness.

According to kinetic theory, the thermal conductivity is defined as $k = (1/3)\sum_{\text{pol}} C v \Lambda_{\text{eff}} \omega$, where C , v , ω , Λ_{eff} are the heat capacity, group velocity, frequency, and the effective mean free path over all phonon polarizations, respectively. The thermal conductivity reduction in solids originates from scattering from grain boundaries, where the mean free path is a function of average grain size and phonon frequency. Further, it also depends on grain boundary structure and impurity atoms at the boundary that affect the phonon transmission and

reflection at each interface.^{54–56} Very recently, it was reported that a substantial reduction in thermal conductivity in FeSb₂ occurs as the grain size decreases from micrometers to nanometers due to dominant scattering from smaller grains.⁵⁷ The porosity and phonon scattering at grain boundaries are found to be the dominant mechanisms for thermal conductivity reduction in nanocrystalline materials.⁵⁸ Isotopic doping and a decrease in the phonon group velocity can also cause reduction in thermal conductivity.^{59,60} In porous materials, thermal conduction through the solid phase, radiation across the pores, and convection through the porous phase, etc. contributes to the effective thermal conductivity. The scattering of phonons by interaction with the surroundings or the presence of defects produced by the surfactant micelles in solutions can also lead to a decrease in the thermal conductivity.⁶¹ Since phonons are scattered at surfaces and interfaces, a reduction in k is anticipated with an increase in the surface-to-volume ratio. Experimental studies show that the excess SDS surfactants on the CNT surface can decrease the thermal conductivity enhancement of nanofluids due to an increase in the interfacial resistance.³³ Assal et al.⁶² also reported a considerable decrease in thermal conductivity of water as the surfactant concentration (CTAB) increases.

It should be noted that the micellar (spherical) size of SDS is much smaller (~ 3.7 nm) than that of CTAB (~ 5 nm), NP9 (~ 6.2 nm), and NP10 (~ 6.8 nm). Therefore, the total interfacial area ($\sim 1/r$ dependence) available for SDS is much larger than the other three. If we invoke the concept of phonon scattering at interfaces, k should decrease with an increase in the surface-to-volume ratio. However, the k decrease was almost the same at high volume fraction for all four surfactants. The average CTAB intermicellar spacing (IPS) reduces from 32 to 2.9 nm as the concentration is increased from $\varphi = 0.002$ to 0.16, where the micellar number density increases from 2.41×10^{22} to 2.43×10^{24} . For NP9, the IPS reduces from 36 to 3.7 nm as the concentration is increased from $\varphi = 0.002$ to 0.16, where the micellar number density increases from 1.58×10^{22} to 1.21×10^{24} . For NP10, the IPS reduces from 41 to 4.2 nm as the concentration is increased from $\varphi = 0.002$ to 0.16, where the micellar number density increases from 1.11×10^{22} to 8.54×10^{23} . For SDS, the IPS reduces from 20 to 2 nm as the concentration is increased from $\varphi = 0.002$ to 0.16, where the micellar number density increases from 8.64×10^{22} to 6.1×10^{24} . Among all four micelles, SDS seems to have the highest number density and lowest IPS. Therefore, SDS is expected to have the maximum thermal conductivity enhancement compared to the other surfactant. But from the experimental results it is clear that the thermal conductivity enhancement for nonionic and cationic surfactant is more compared to that of SDS of the same volume fraction. This may be due to the fact that the number of micelles present in the system for the same surfactant concentration is more in the case of nonionic and cationic surfactant compared to that of SDS, since the cmc for SDS is 8×10^{-3} M, whereas for CTAB, NP9, and NP10 the cmc values are 9×10^{-4} , 6×10^{-5} , and 7×10^{-5} M, respectively. Therefore, the number of holes (disorder) in the systems studied follows the trend NP10 \approx NP9 > CTAB > SDS for the same volume fraction. Hence the decrease in thermal conductivity should be more for nonionic surfactant compared to cationic and anionic system, which was consistent with our experimental results.

3.3. Effect of Concentration of Dispersed Phase on Interfacial Tension. To study the effect of interfacial tension,

the contact angle measurements were carried out for all the four surfactant solutions on a stainless steel substrate. Steel substrate is chosen because the hotwire probe used in our experiment also has a stainless steel body. Figure 7a shows the

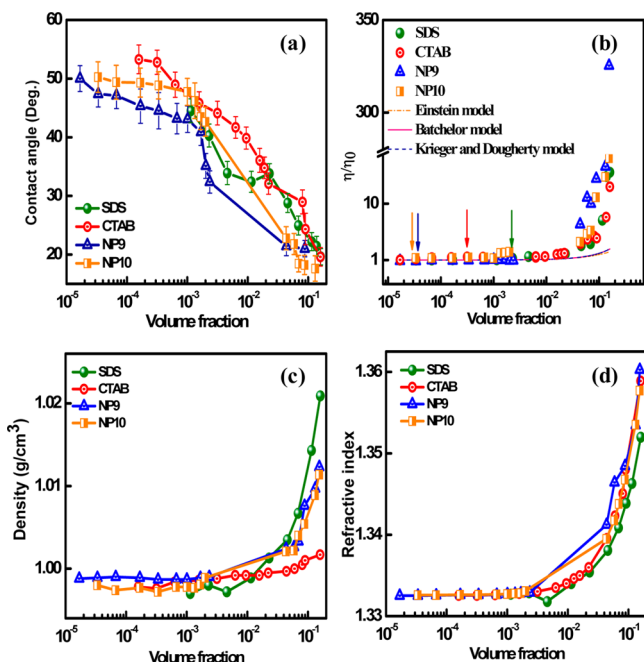


Figure 7. (a) Contact angle as a function of volume fraction of soft spheres. (b) The reduced viscosity as a function of volume fraction along with the theoretical fits using the Einstein, Batchelor, and Krieger and Dougherty models (The cmc values of each surfactant are shown by arrows of respective symbol colors). (c) Density and (d) refractive index as functions of surfactant concentration for SDS, CTAB, NP9, and NP10.

variation of contact angle as a function of concentration of surfactant solutions. As the surfactant concentration increases, the contact angle is found to decrease for all four surfactant solutions.

It is known that the addition of surfactant in water reduces its surface tension or interfacial tension and causes it to spread on a substrate. The relationship between interfacial tension and contact angle is given by $\gamma^{\text{sl}} = \gamma^{\text{sv}} - \gamma^{\text{lv}} \cos \theta$, where γ^{sl} , γ^{sv} , and γ^{lv} are the solid–liquid, solid–vapor, and liquid–vapor interfacial tensions, respectively.

γ_{lv} is calculated using the following formula:⁶⁴

$$\cos \theta = -1 + \sqrt{\frac{\gamma^{\text{sv}}}{\gamma^{\text{lv}}}} e^{-0.0001247(\gamma^{\text{lv}} - \gamma^{\text{sv}})^2} \quad (2)$$

On conversion of the solid to liquid surface tension using the above equations, the solid–liquid interfacial tension for SDS at $\varphi = 0.002$ is 1.625 mJ/m^2 , which reduces to 0.225 mJ/m^2 at a $\varphi = 0.09$. Similarly, the interfacial tension of CTAB, NP9, and NP10 solutions decreased from 2.734 to 0.228, 0.913 to 0.074, and 1.98 to 0.06 mJ/m^2 , respectively, as the surfactant concentration decreases from $\varphi = 0.02$ to 0.09. From our contact angle measurements, the calculated value of γ^{sl} for water is 72.7 mJ/m^2 , which is in good agreement with the reported value of 72.75 mJ/m^2 .⁶⁵ The reported value of γ^{sl} for CTAB on mica substrate is $1.5 \pm 1 \text{ mJ/m}^2$ at one cmc concentration.⁶⁶ This clearly shows that the presence of surfactant micelles makes the fluid more hydrophilic. Theoretical studies show that

R_b attains relatively larger value only when the liquid is more hydrophobic than the solid surface.⁶⁷ Studies show that the orientation of adsorbed moieties of nonionic surfactants changes with surfactant concentrations, which can result in changes in the free energy of adsorption.⁶⁸ An earlier study shows that the thermal conductivity of zinc sulfide is increased when large particles of highly conducting diamond are added, but k lowered when submicrometer size particles are added, which was explained by the change in interfacial thermal resistance at larger surface to volume ratio.⁶⁹ According to the Debye model $R_{\text{Bd}} = 4/(\rho C v \eta)$, where R_{Bd} is the phonon boundary resistance, ρ is the density, C is the specific heat, v is the Debye velocity of the matrix, and q is the average probability for the transmission of the phonons across the interface into the particles. Therefore, thermal conductivity of the dispersion is $K_m = (1/3)\rho C v l$ where l is the phonon mean free path. Therefore, the Kapitza radius a_k ($\sim 1/q$) depends on the probability of phonon crossing at the interface. When the particle size is less than the Kapitza radius, the effective conductivity of the dispersion is lowered by the particles.

3.4. Effect of Concentration of Dispersed Phase on Viscosity Enhancement.

Figure 7b shows the reduced viscosity (η/η_0) as a function of surfactant concentration for SDS, CTAB, NP9, and NP10. In all the four systems, the viscosity increase was nominal up to 0.05 (φ). The percentage of enhancement in viscosity at $\varphi = 0.002$ was 7, 13, 3 and 40% for SDS, CTAB, NP9, and NP10, respectively. Further increase in the concentration of the surfactant leads to a dramatic enhancement in reduced viscosity for all the four surfactants. The reduced viscosity values at $\varphi = 0.08$ for SDS, CTAB, NP9, and NP10 are 1.95, 2.65, 27.59, and 13.03, respectively. What is the reason for the observed sharp increase in viscosity above a certain surfactant concentration? The large increase in the viscosity above 0.08 volume fraction of surfactant solutions can be understood in terms of the structural changes of the micelles. It is known that upon increasing surfactant concentration well beyond the cmc, the motion of charged micelles is inhibited by this crowding, and the hydrated spherical micelles are deformed to rod-shaped micelles, resulting in an increase in viscosity.⁴² A sphere to rod transition in SDS solution occurs at a concentration of 0.25 mol/L ($\sim \varphi = 0.07$) at a temperature of 27°C .⁷⁰ The reported value of the aggregation number of SDS spherical micelle is 60 and for rod-shaped micelles [formed above $\varphi = 0.07$ with a semiminor axis of 17 \AA ($b = c$) and semimajor axis of 35.8 \AA] is approximately 106.⁷¹ In the case of CTAB, the sphere to rod transition will occur at a concentration above $\varphi = 0.075$.^{42,72} The dramatic increase in the viscosity observed in SDS and CTAB micellar solution above $\varphi = 0.08$ confirms the formation of rod-shaped micelles that are randomly packed. Such a sharp increase in the viscosity of the surfactant solution due to the formation of rod-like micelles was reported earlier.⁷¹ A similar dramatic increase in viscosity due to rod-shaped micelles is observed for NP9 and NP10 systems, above $\varphi = 0.07$. In general, the viscosity data follows the Einstein model at dilute concentrations, where it assumes that the particles are rigid, uncharged, without attractive forces, and small enough so that the dilatational perturbation of the flow is unbounded to decay to zero.⁷³ A particle moves at the velocity of the streamline in line with the particle center in such a suspension. The Einstein equation describes the dependence of viscosity increase with concentration of particles in the simplest case of dilute suspensions ($\varphi \leq 0.01$) as $\eta/\eta_0 = 1 + 2.5\varphi$, where φ is the particle volume

fraction, η is the nanofluid dynamic viscosity, and η_0 the base fluid dynamic viscosity. For $\varphi \geq 0.01$, hydrodynamic interactions between particles become important as the disturbance of the fluid around one particle interacts with those around other particles. The viscosity in such a case is given by the Batchelor equation: $\eta/\eta_0 = 1 + 2.5\varphi + 6.5\varphi^2$.⁷⁴ For $\varphi \geq 0.1$, the multiparticle collisions become increasingly important, and a semiempirical relationship for the shear viscosity covering a full range of particle volume fractions was obtained by Krieger and Dougherty, $\eta/\eta_0 = [1 - (\varphi/\varphi_m)]^{-[\eta]\varphi_m}$,⁷⁵ where, $[\eta]$ is the intrinsic viscosity, which is 2.5 for hard spheres, and φ_m is the maximum packing fraction. For randomly monodispersed spheres, the maximum close packing fraction is approximately 0.64.

The Einstein, Batchelor, and Krieger–Dougherty (KD) fits on the experimental data points are shown in the Figure 7b. The results show that the enhancement in viscosity ratio with φ is much more than the values predicted by models at relatively large volume fractions. Since the number density increases with concentration, the interaction between the micelles at higher concentration becomes stronger, which has contributed to the observed deviation from the theoretical fit. It should be noted that the effectiveness of the nanofluid coolants depends on the flow modes (laminar or turbulent). Lower viscosity implies lower pumping power, which is advantageous from an industrial application standpoint. A quantitative expression derived for fully developed laminar flow that compares the relative coefficients of viscosity and k enhancement shows that the use of nanofluid will be beneficial if the increase in the viscosity is less than 4 times the increase in k . Viscosity and thermal conductivity enhancements can be described by linear dependence on the particle volume fraction as $k/k_f = 1 + C_k\varphi$ and $\eta/\eta_0 = 1 + C_\eta\varphi$, where C_k and C_η are constants. At low volume fractions, for the nanofluid to be beneficial, the ratio of coefficients (C_η/C_k) should be <4.93 . At $10 \times \text{cmc}$ (and $30 \times \text{cmc}$), the ratio of viscosity to thermal conductivity increase for SDS, CTAB, and NP9 are -6 (and -13), -3.7 (and -2.8), and 0.39 (and -0.26), respectively. These results suggest that the cationic and nonionic surfactants are better emulsifiers for optimal thermal to rheological property enhancements.

3.5. Effect of Surface Morphologies on k , Viscosity, Density and Refractive Index. The viscosity measurements clearly show that a morphological change (sphere to rod transition) occurs in the case of all the surfactants above $\varphi = 0.07$. It may be seen from Figure 6 that the k is reduced drastically after $\varphi = 0.07$, which may be due to the sphere to rod transition. Figure 7c,d shows the density and the refractive index variation as a function of surfactant concentration for SDS, CTAB, NP9, and NP10. The morphological transitions in the surfactant solutions above $\varphi = 0.08$ are also evident in the density and refractive index measurements. From Figure 7c, it is seen that the density increases from 1.0013 to 1.0143 g/cm^3 as the concentration of SDS increases from $\varphi = 0.002$ to 0.08 . Similarly, in the case of CTAB, the density increases from 0.9988 to 1.0005 g/cm^3 , while in the case of NP9, it increases from 0.999 to 1.0076 g/cm^3 for an increase in $\varphi = 0.002$ to 0.08 . For the same increase in volume fraction, the density of NP10 increases from 0.9989 to 1.0054 g/cm^3 . The large variation in the density of surfactant solutions above 0.08φ further corroborates the formation of rod-shaped micelles. The refractive index (Figure 7d) of the solutions also shows a systematic increase with concentration of surfactants in all four

cases. Again, a dramatic increase in the refractive index is observed above 0.08φ .

In the microconvection model, the convection velocity is taken to be the root-mean-square (rms) velocity of the nanoparticle. The root-mean-square velocity (v_N) of a Brownian particle can be defined as $v_N = [(18k_B T)/(\pi\rho d^3)]^{1/3}$ where k_B is the Boltzmann constant, T the temperature, ρ the density, and d the diameter of the nanoparticle. Considering the micellar size, the maximum convection velocity is expected in SDS (size $\sim 2.5 \text{ nm}$) and the least in NP9 (size $\sim 6.5 \text{ nm}$). Therefore, in terms of microconvection theory, the observed negative enhancement in k with volume fractions is consistent. However, it is intriguing that the effective medium theory holds good even after the morphological transformation (spherical to cylindrical micellar). Studies show that the cylindrical structure with large aspect ratio enhances the thermal conductivity of nanofluids compared to the spherical ones.⁷⁶ The aspect ratio of the suspended particles and the orientation of the particles with respect to the heat flow direction play a crucial role in k enhancement. In the case of magnetic nanofluids with large aspect ratio, alignment of nanostructures along the field direction can cause dramatic enhancement in the thermal properties due to the parallel mode of conduction.⁷⁷ It should be noted that the aspect ratio, in the case of magnetic nanofluids, increases several orders of magnitude when they are subjected to a magnetic field. However, aspect ratio change in the case of surfactant micelles after transformation from a spherical to cylindrical micelle is very small. In the case of SDS at 0.07 vol\% , the semiminor and major axis are 1.7 and 3.58 nm , respectively.⁷¹ Probably, the small changes in the aspect ratio and the lower k of micelles have contributed to the observed good agreement between the experimental data and EMT prediction. On the basis of our results, the possible thermal resistance contributions from different moieties of the micelles (headgroup, tail, and water molecules) are schematically shown in the inset in Figure 6. The maximum interfacial resistance is offered by the hydrophobic tail part and the minimum by the fluid molecules.

3.6. Effect of Surfactant on k Enhancement in Aqueous and Nonaqueous Metal Oxide Nanofluid.

3.6.1. Aqueous Alumina Nanofluid. Figure 8 shows the variation of k/k_f as a function of φ of Al_2O_3 nanofluids without surfactant and with surfactants CTAB and NP9 of 10 and $70 \times \text{cmc}$. The k/k_f for pure surfactants of CTAB and NP9 of same volume fractions (10 and $70 \times \text{cmc}$) are also shown in the Figure 8 for comparison. The best fit using effective medium theory is shown by the solid line. Over all, the experimental data fit fairly well with the EMT theory for various volume fractions of alumina nanofluids with and without surfactants, except for a small deviation at higher volume fractions. The maximum thermal conductivity enhancement for nanofluids with a particle loading of 0.06 was $\sim 14.4\%$. The most striking observation was that though the k/k_f of the surfactant micellar solutions was lower than that of the base fluid, the k/k_f of the nanofluids with the same amount of soft spheres (micelles) is dictated by the thermal conductivity of nanofluids. This is a very promising result in terms of industrial applications of surfactant stabilized nanofluids. To verify these intriguing results, the experiments are repeated for other nanofluids too. The schematic representation of the system containing charged Al_2O_3 nanoparticles and surfactant micelles is depicted in the inset of Figure 8.

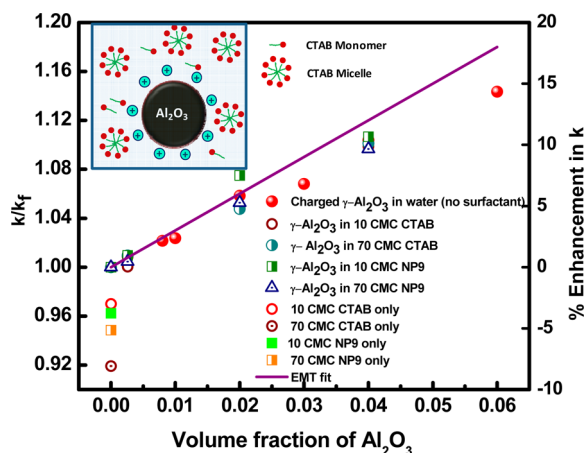


Figure 8. The variation of k/k_f as a function of alumina nanoparticle volume fraction without and with CTAB and NP9 along with the theoretical fit using (solid line) EMT. The inset shows the schematics of charged γ - Al_2O_3 in CTAB micellar solution.

3.6.2. Aqueous Silica Nanofluid. Figure 9 shows the variation of k/k_f as a function of ϕ of SiO_2 nanofluids without

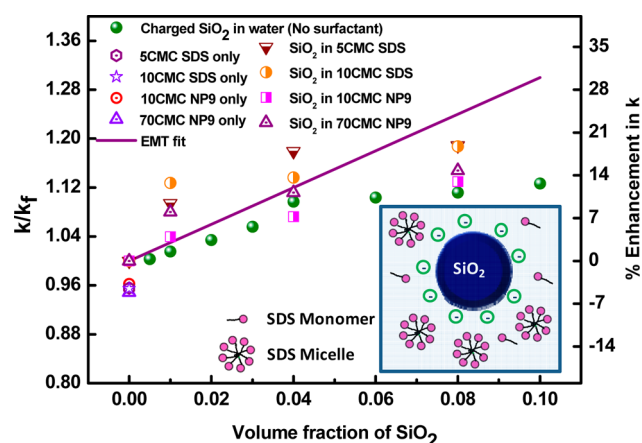


Figure 9. The variation of k/k_f as a function of SiO_2 nanoparticle volume fraction without and with SDS and NP9 along with the theoretical fit (solid line) using EMT. The inset shows the schematics of charged SiO_2 in SDS micellar solution.

surfactant and with surfactants SDS and NP9 of 5, 10, and $70 \times \text{cmc}$. The k/k_f for pure surfactants of SDS and NP9 of same volume fractions (5, 10, and $70 \times \text{cmc}$) are also shown in the Figure 9 for comparison. The best fit using effective medium theory is shown by the solid line. The experimental data fit fairly well with the EMT theory up to 0.04 volume fraction of SiO_2 with and without surfactants, and the fit was poor at higher volume fractions. The maximum thermal conductivity enhancement for nanofluids with a particle loading of 0.1 was $\sim 12.6\%$. Again, the k/k_f of the nanofluids with the same amount of soft spheres is dictated by the thermal conductivity of the nanofluids. The schematic representation of the system containing charged SiO_2 nanoparticles and surfactant micelles is depicted in the inset of Figure 9.

3.6.3. Nonaqueous Fe_3O_4 Nanofluid. Figure 10 shows the variation of k/k_f as a function of ϕ of Fe_3O_4 nanofluids with coated 10% oleic acid surfactant and 5 and 10 wt % of surfactant in base fluid (kerosene). The best fit using effective medium theory is shown by the solid line. The experimental

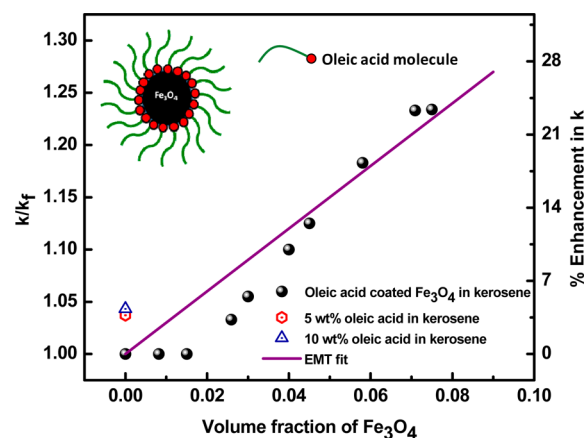


Figure 10. The variation of k/k_f as a function of Fe_3O_4 nanoparticle volume fraction along with the theoretical fit (solid line) using EMT. The inset schematic shows the oleic acid-coated Fe_3O_4 particle.

data fit fairly well with the EMT theory, especially above 0.04 volume fraction of Fe_3O_4 . The maximum thermal conductivity enhancement for nanofluids with a particle loading of 0.08 was $\sim 23.4\%$. These results were consistent with the k enhancement observed in magnetic nanofluids, without external magnetic field.²¹ On the contrary, very large enhancement in k is observed under magnetic field due to a parallel mode of conduction. Again, the k/k_f of base fluid with the same amount of surfactant alone shows much lower value compared to the one with nanoparticles. The carboxylic acid group of oleic acid binds to the magnetite, while the aliphatic chain extends out into the nonpolar solvent, thus providing steric hindrance between the particles. The charge at the carboxylate ion of oleic acid delocalizes in between two oxygen atoms because of the resonance effect. The surfactant coating thus prevents the agglomeration of particles against van der Waals and magnetic attractive interactions. Besides, it passivates the nanocrystals against further oxidation. These results confirm that the thermal conductivity of nanofluid is dictated by the thermal conductivity of suspended particles. The schematic of the nanoparticles with adsorbed surfactant moieties is depicted in the inset of Figure 10.

Thermal conductivity values of bulk particle, base fluid, and nanofluids of different volume fractions and their respective percentage enhancement are shown in Table 1. With and without surfactant, the k/k_f enhancement was almost the same in the case of alumina, silica, and iron oxide nanofluids. It can be seen that the value of k/k_f enhancement with pure surfactant was negative, while it is positive at all concentrations of nanoparticles for all the three systems. In general, the excess surfactant did not show a lowering of k of the nanofluid, though the surfactant alone in base fluids showed a negative enhancement. For example, SiO_2 nanofluid of 0.08 ϕ shows an enhancement of 13% without any surfactant and an 18% enhancement with SDS. This shows that the thermal conductivity of a nanofluid in the presence of surfactant and nanoparticles simply follows the thermal conductivity of nanoparticles in the fluid, and the addition of surfactant, even beyond the optimal concentration, would not lower the thermal conductivity of nanofluids significantly. Besides, the surfactant moieties on nanoparticles aid thermal conductivity enhancement and also improve the stability of nanofluids against agglomeration of suspended particles.

Table 1. Thermal Conductivity of Bulk Particle, Base Fluid, and Thermal Conductivity Ratio of Nanofluid of Different Volume Fraction and Their Corresponding Percent Enhancement

sample no.	material	thermal conductivity of bulk particle (W/m K)	base fluid	thermal conductivity of base fluid (W/m K)	thermal conductivity ratio of nanofluid	% enhancement
1	Fe ₃ O ₄	9.7	kerosene	0.116	1.03 ($\phi = 0.02$)	3
					1.1 ($\phi = 0.04$)	10
					1.18 ($\phi = 0.06$)	18
					1.23 ($\phi = 0.07$)	23
2	Al ₂ O ₃	35	water	0.6	1.09 ($\phi = 0.02$)	9
					1.10 ($\phi = 0.04$)	10
					1.14 ($\phi = 0.06$)	14
					1.03 ($\phi = 0.02$)	3
3	SiO ₂	1.4	water	0.6	1.09 ($\phi = 0.04$)	9
					1.10 ($\phi = 0.06$)	10
					1.13 ($\phi = 0.08$)	13

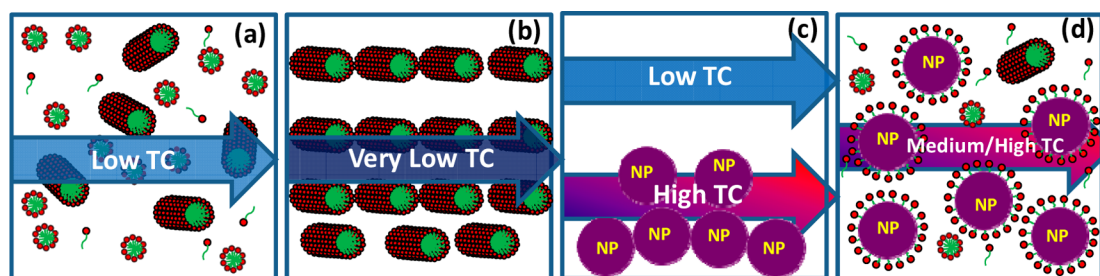
**Figure 11.** Schematic representation of nanofluids: (a) soft system with spherical and cylindrical micelles randomly arranged ($k_p < k_f$), (b) aligned cylindrical micelles ($k_p < k_f$), (c) bare nanoparticle in base fluid ($k_p \gg k_f$), and (d) surfactant-coated nanoparticle in base fluid ($k_p \gg k_f$).

Figure 11 shows the schematic representation of nanofluids based on the experimental findings. Figure 11a depicts a soft micellar system with spherical and cylindrical micelles randomly arranged ($k_p < k_f$). This scenario arises when the surfactant concentration is above the critical micellar concentration (cmc). Because $k_p < k_f$, the system shows a $k/k_f < 1$. Figure 11b renders aligned cylindrical micelles at extremely large concentrations of surfactants ($c \gg \text{cmc}$). Again, because $k_p < k_f$, the system shows a $k/k_f < 1$. Figure 11c represents nanoparticles in base fluid ($k_p \gg k_f$) where no surface active species are used. Due to agglomeration and subsequent settling, the heavy nanoparticles settle at the bottom of the container. Here, two different conduction pathways are possible, one through the nanoparticle pathway, where the k/k_f is high, and the other through the liquid pathway, where the k/k_f is low. Figure 11d portrays surfactant-coated nanoparticle in base fluid ($k_p \gg k_f$). Here, the surfactant moieties stabilize the nanoparticles, thereby providing a stable suspension, where the k/k_f enhancement will be modest or high. However, conduction through percolating nanoparticle paths can carry heat much more effectively.⁴⁴

4. CONCLUSIONS

The thermal properties of nanofluids containing soft spheres of surfactants with different headgroup charges and alkyl chain lengths are investigated. The contributions of interfacial resistance, density, viscosity, and surface morphology of dispersed particles on thermal conductivity are also studied by using model soft systems of micelles in the size range of 2.5–7 nm. Our results show that the thermal conductivity variation of surfactant micelles with volume fraction fits well with the effective medium theory of poor thermal conductors. The long alkyl chain group of nonionic surfactant micelles is

found to be a very poor thermal conductor at very low concentrations, with large interfacial tension compared to their anionic counterparts. Though a dramatic enhancement in viscosity is noticed at high concentrations due to transformation of spherical micelles into cylindrical, the effective medium theory holds good even after the morphological transformation. This may be due to the minor changes in the aspect ratio and poor k of micelles as such. The k measurement in alumina, silicon dioxide, and iron oxide nanofluids in the presence of ionic and nonionic surfactants shows that the adsorbed surfactant does not influence the thermal conductivity enhancement in nanofluids. Further, the stabilizing moieties on nanoparticles do not reduce the thermal properties of nanofluids but enhance the dispersibility and stability of nanoparticles in base fluids. These findings will have important implications for producing efficient nanofluids with superior heat transfer properties.

AUTHOR INFORMATION

Corresponding Author

*Phone: 00-91-9443151536. Fax: 91-44-27480356. E-mail: philip@igcar.gov.in.

Notes

The authors declare no competing financial interest.

ACKNOWLEDGMENTS

Authors would like to thank Dr. T. Jayakumar and Dr. P. R. Vasudeva Rao for useful discussions. J.P. thanks BRNS for a perspective research grant for advanced nanofluid development program.

REFERENCES

- (1) Fang, J.; Kang, C. B.; Huang, Y.; Tolbert, S. H.; Pilon, L. Thermal conductivity of ordered mesoporous nanocrystalline silicon thin films made from magnesium reduction of polymer-templated silica. *J. Phys. Chem. C* **2012**, *116* (23), 12926–12933.
- (2) Alaghemandi, M.; Gharib-Zahedi, M. R.; Spohr, E.; Boehm, M. C. Thermal conductivity of polyamide-6,6 in the vicinity of charged and uncharged graphene layers: A molecular dynamics analysis. *J. Phys. Chem. C* **2012**, *116* (26), 14115–14122.
- (3) Eastman, J. A.; Choi, S. U. S.; Li, S.; Yu, W.; Thompson, L. J. Anomalous increased effective thermal conductivities of ethylene glycol-based nanofluids containing copper nanoparticles. *Appl. Phys. Lett.* **2001**, *78*, 718–720.
- (4) Gharagozloo, P. E.; Eaton, J. K.; Goodson, K. E. Diffusion, aggregation, and the thermal conductivity of nanofluids. *Appl. Phys. Lett.* **2008**, *93*, 103110.
- (5) Wright, B.; Thomas, D.; Hong, H.; Groven, L.; Puszynski, J.; Duke, E.; Ye, X.; Jin, S. Magnetic field enhanced thermal conductivity in heat transfer nanofluids containing Ni coated single wall carbon nanotubes. *Appl. Phys. Lett.* **2007**, *91*, 173116.
- (6) Li, C. H.; Peterson, G. P. The effect of particle size on the effective thermal conductivity of Al_2O_3 –water nanofluids. *J. Appl. Phys.* **2007**, *101*, 044312.
- (7) Eapen, J.; Williams, W. C.; Buongiorno, J.; Hu, L. W.; Yip, S.; Rusconi, R.; Piazza, R. Mean-field versus microconvection effects in nanofluid thermal conduction. *Phys. Rev. Lett.* **2007**, *99*, 095901.
- (8) Rusconi, R.; Rodari, E.; Piazza, R. Optical measurements of the thermal properties of nanofluids. *Appl. Phys. Lett.* **2006**, *89*, 261916.
- (9) Kim, S. J.; Bang, I. C.; Buongiorno, J.; Hu, L. W. Effects of nanoparticle deposition on surface wettability influencing boiling heat transfer in nanofluids. *Appl. Phys. Lett.* **2006**, *89*, 153107.
- (10) Buongiorno, J. Convective transport in nanofluids. *J. Heat Transfer* **2006**, *128* (3), 240–250.
- (11) Keblinski, P.; Eastman, J. A.; Cahill, D. G. Nanofluids for thermal transport. *Mater. Today* **2005**, *8*, 36–44.
- (12) Younes, H.; Christensen, G.; Luan, X.; Hong, H.; Smith, P. Effects of alignment, pH, surfactant, and solvent on heat transfer nanofluids containing Fe_2O_3 and CuO nanoparticles. *J. Appl. Phys.* **2012**, *111*, 064308.
- (13) Gao, T.; Jelle, B. P. Thermal conductivity of TiO_2 nanotubes. *J. Phys. Chem. C* **2013**, *117* (3), 1401–1408.
- (14) Huang, X.; Zhi, C.; Jiang, P. Toward effective synergetic effects from graphene nanoplatelets and carbon nanotubes on thermal conductivity of ultrahigh volume fraction nanocarbon epoxy composites. *J. Phys. Chem. C* **2012**, *116*, 23812–23820.
- (15) Nanda, J.; Maranville, C.; Bollin, S. C.; Sawall, D.; Ohtani, H.; Remillard, J. T.; Ginder, J. M. Thermal conductivity of single-wall carbon nanotube dispersions: Role of interfacial effects. *J. Phys. Chem. C* **2008**, *112*, 654–658.
- (16) Zhu, H. T.; Zhang, C. Y.; Tang, Y. M.; Wang, J. X. Novel synthesis and thermal conductivity of CuO nanofluid. *J. Phys. Chem. C* **2007**, *111*, 1646–1650.
- (17) Aravind, S. S. J.; Baskar, P.; Baby, T. T.; Sabareesh, R. K.; Das, S.; Ramaprabhu, S. Investigation of structural stability, dispersion, viscosity, and conductive heat transfer properties of functionalized carbon nanotube based nanofluids. *J. Phys. Chem. C* **2011**, *115*, 16737–16744.
- (18) Murshed, S. M. S.; Castro, C. A. N. d.; Lourenco, M. J. V. Effect of surfactant and nanoparticle clustering on thermal conductivity of aqueous nanofluids. *J. Nanofluids* **2012**, *1* (2), 175–179.
- (19) Hong, H.; Wensel, J.; Smith, P. Evidences of aggregation between metal oxide nanoparticles and carbon nanotubes in heat transfer nanofluids. *J. Nanofluids* **2013**, *2* (1), 38–44.
- (20) Buongiorno, J.; Venerus, D. C.; Prabhat, N.; McKrell, T.; Townsend, J.; Christianson, R.; Tolmachev, Y. V.; Keblinski, P.; Hu, L.-w.; Alvarado, J. L.; Bang, I. C.; Bishnoi, S. W.; Bonetti, M.; Botz, F.; Cecere, A.; Chang, Y.; Chen, G.; Chen, H.; Chung, S. J.; Chyu, M. K.; Das, S. K.; Paola, R. D.; Ding, Y.; Dubois, F.; Dzido, G.; Eapen, J.; Escher, W.; Funfschilling, D.; Galand, Q.; Gao, J.; Gharagozloo, P. E.; Goodson, K. E.; Gutierrez, J. G.; Hong, H.; Horton, M.; Hwang, K. S.; Iorio, C. S.; Jang, S. P.; Jarzebski, A. B.; Jiang, Y.; Jin, L.; Kabelac, S.; Kamath, A.; Kedzierski, M. A.; Kieng, L. G.; Kim, C.; Kim, J.-H.; Kim, S.; Lee, S. H.; Leong, K. C.; Manna, I.; Michel, B.; Ni, R.; Patel, H. E.; Philip, J.; Poulikakos, D.; Reynaud, C.; Savino, R.; Singh, P. K.; Song, P.; Sundararajan, T.; Timofeeva, E.; Tritcak, T.; Turanov, A. N.; Vaerenbergh, S. V.; Wen, D.; Witharana, S.; Yang, C.; Yeh, W.-H.; Zhao, X.-Z.; Zhou, S.-Q. A benchmark study on the thermal conductivity of nanofluids. *J. Appl. Phys.* **2009**, *106*, 094312.
- (21) Philip, J.; Shima, P. D.; Raj, B. Enhancement of thermal conductivity in magnetite based nanofluid due to chainlike structures. *Appl. Phys. Lett.* **2007**, *91*, 203108.
- (22) Shalkevich, N.; Shalkevich, A.; Burgi, T. Thermal conductivity of concentrated colloids in different states. *J. Phys. Chem. C* **2010**, *114*, 9568–9572.
- (23) Komati, S.; Suresh, A. K. Anomalous enhancement of interphase transport rates by nanoparticles: Effect of magnetic iron oxide on gas–liquid mass transfer. *Ind. Eng. Chem. Res.* **2010**, *49*, 390–405.
- (24) Prasher, R.; Evans, W.; Meakin, P.; Fish, J.; Phelan, P.; Keblinski, P. Effect of aggregation on thermal conduction in colloidal nanofluids. *Appl. Phys. Lett.* **2006**, *89*, 143119.
- (25) Gao, J. W.; Zheng, R. T.; Ohtani, H.; Zhu, D. S.; Chen, G. Experimental investigation of heat conduction mechanisms in nanofluids. Clue on clustering. *Nano Lett.* **2009**, *9*, 4128–4132.
- (26) Murshed, S. M. S.; Castro, C. A. N. d. Predicting the thermal conductivity of nanofluids—Effect of Brownian motion of nanoparticles. *J. Nanofluids* **2012**, *1* (2), 180–185.
- (27) Gorla, R. S. R.; Kumari, M. Mixed convection flow of a non-Newtonian nanofluid over a non-linearly stretching sheet. *J. Nanofluids* **2012**, *1* (2), 186–195.
- (28) Huang, X.; Iizuka, T.; Jiang, P.; Ohki, Y.; Tanaka, T. Role of interface on the thermal conductivity of highly filled dielectric epoxy/ AlN composites. *J. Phys. Chem. C* **2012**, *116*, 13629–13639.
- (29) Wei, Z.; Ni, Z.; Bi, K.; Chen, M.; Chen, Y. Interfacial thermal resistance in multilayer graphene structures. *Phys. Lett. A* **2011**, *375*, 1195–1199.
- (30) Timofeeva, E. V.; Smith, D. S.; Yu, W.; France, D. M.; Singh, D.; Routbort, J. L. Particle size and interfacial effects on thermo-physical and heat transfer characteristics of water-based α -SiC nanofluids. *Nanotechnology* **2010**, *21*, 215703.
- (31) Zhou, X. F.; Gao, L. Effective thermal conductivity in nanofluids of nonspherical particles with interfacial thermal resistance: Differential effective medium theory. *J. Appl. Phys.* **2006**, *100*, 024913.
- (32) Yu, W.; Choi, S. U. S. The role of interfacial layers in the enhanced thermal conductivity of nanofluids: A renovated Hamilton–Crossover model. *J. Nanopart. Res.* **2004**, *6*, 355–361.
- (33) Huxtable, S. t.; Cahill, D. G.; Shenogin, S.; Xue, L.; Ozisik, R.; Barone, P.; Usrey, M.; Strano, M. S.; Siddons, G.; Shim, M.; Keblinski, P. Interfacial heat flow in carbon nanotube suspensions. *Nat. Mater.* **2003**, *2*, 731–734.
- (34) Yang, H. S.; Bai, G. R.; Thompson, L. J.; Eastman, J. A. Interfacial thermal resistance in nanocrystalline yttria stabilized zirconia. *Acta Mater.* **2002**, *50* (9), 2309–2317.
- (35) Nan, C. W.; Birringer, R.; Clarke, D. R.; Gleiter, H. Effective thermal conductivity of particulate composites with interfacial thermal resistance. *J. Appl. Phys.* **1997**, *81*, 6692–6699.
- (36) Sato, K.; Fujimoto, K.; Kawamura, K.; Dai, W.; Hunger, M. Rheological mechanism of long-term self-assembly in saponite nanoparticles. *J. Phys. Chem. C* **2012**, *116* (43), 22954–22959.
- (37) Duplatre, G.; Marques, M. F. F.; Miguel, M. d. G. Size of sodium dodecyl sulfate micelles in aqueous solutions as studied by positron annihilation lifetime spectroscopy. *J. Phys. Chem.* **1996**, *100*, 16608–16612.
- (38) Wu, C.; Ma, R.; Zhou, B.; Shen, J.; Chan, K. K.; Woo, K. F. Laser light-scattering study of the dendritic-like polyelectrolytes and CTAB complex formation. *Macromolecules* **1996**, *29*, 228–232.
- (39) Mata, J. P.; Aswal, V. K.; Hassan, P. A.; Bahadur, P. A phenol-induced structural transition in aqueous cetyltrimethylammonium bromide solution. *J. Colloid Interface Sci.* **2006**, *299*, 910–915.

- (40) Bagwe, R. P.; Mishra, B. K.; Khilar, K. C. Effect of chain length of oxyethylene group on particle size and absorption spectra of silver nanoparticles prepared in non-ionic water-in-oil micro emulsion. *J. Dispersion Sci. Technol.* **2012**, *20* (6), 1569–1579.
- (41) Os, N. M. V.; Haak, J. R.; Rupert, L. A. M. *Physico-Chemical Properties of Selected Anionic, Cationic and Nonionic Surfactants*; Elsevier Science: Amsterdam, 1993; p 608.
- (42) Ekwall, P.; Mandell, L.; Solyom, P. The aqueous cetyl trimethylammonium bromide solutions. *J. Colloid Interface Sci.* **1971**, *35* (4), 519–528.
- (43) Lindmann, B.; Olofsson, G.; Stenius, P. *Surfactants, Adsorption, Surface Spectroscopy and Disperse Systems*; Springer: Darmstadt, Germany, 1985; p 128.
- (44) Shima, P. D.; Philip, J.; Raj, B. Synthesis of aqueous and nonaqueous iron oxide nanofluids and study of temperature dependence on thermal conductivity and viscosity. *J. Phys. Chem. C* **2010**, *114* (44), 18825–18833.
- (45) Costa, T. M. H.; Gallas, M. R.; Benvenuti, E. V.; Jornada, J. A. H. d. Study of nanocrystalline γ - Al_2O_3 produced by high-pressure compaction. *J. Phys. Chem. B* **1999**, *103*, 4278–4284.
- (46) Anderson, D. R. Thermal conductivity of polymer. *Chem. Rev.* **1966**, *66* (6), 677–690.
- (47) Mueller, F. H.; Houwink, R. *Chemie und Technologie der Kunststoffe*; Akademische Verlagsgesellschaft: Leipzig, Germany, 1942.
- (48) Maxwell, J. C. *A Treatise on Electricity and Magnetism*, 2nd ed.; Clarendon Press: Oxford, 1881.
- (49) Hashin, Z.; Shtrikman, S. A variational approach to the theory of the effective magnetic permeability of multiphase materials. *J. Appl. Phys.* **1962**, *33*, 3125–3131.
- (50) Vladkov, M.; Barrat, J. L. Modelling transient absorption and thermal conductivity in a simple nanofluid. *Nano Lett.* **2006**, *6* (6), 1224–1228.
- (51) Evans, W.; Fish, J.; Keblinski, P. Role of Brownian motion hydrodynamics on nanofluid thermal conductivity. *Appl. Phys. Lett.* **2006**, *88*, 093116.
- (52) Eapen, J.; Li, J.; Yip, S. Beyond the Maxwell limit: Thermal conduction in nanofluids with percolating fluid structures. *Phys. Rev. E* **2007**, *76*, 062501.
- (53) Wang, B. X.; Zhou, L. P.; Peng, X. F. A fractal model for predicting the effective thermal conductivity of liquid with suspension of nanoparticles. *Int. J. Heat Mass Transfer* **2003**, *46* (14), 2665–2672.
- (54) Zhao, H.; Freund, J. B. Phonon scattering at a rough interface between two fcc lattices. *J. Appl. Phys.* **2009**, *105*, 013515.
- (55) Aubry, S.; Kimmer, C. J.; Skye, A.; Schelling, P. K. Comparison of theoretical and simulation-based predictions of grain-boundary Kapitza conductance in silicon. *Phys. Rev. B* **2008**, *78*, 064112.
- (56) Schelling, P. K.; Phillpot, S. R.; Keblinski, P. Kapitza conductance and phonon scattering at grain boundaries by simulation. *J. Appl. Phys.* **2004**, *95* (11), 6082–6091.
- (57) Zhao, H.; Pokharel, M.; Zhu, G.; Chen, S.; Lukas, K.; Jie, Q. Dramatic thermal conductivity reduction by nanostructures for large increase in thermoelectric figure-of-merit of FeSb_2 . *Appl. Phys. Lett.* **2011**, *99*, 163101.
- (58) Wang, Z.; Alaniz, J. E.; Jang, W.; Garay, J. E.; Dames, C. Thermal conductivity of nanocrystalline silicon: Importance of grain size and frequency-dependent mean free paths. *Nano Lett.* **2011**, *11*, 2206–2213.
- (59) Yang, N.; Zhang, G.; Li, B. Ultralow thermal conductivity of isotope-doped silicon nanowires. *Nano Lett.* **2007**, *8* (1), 276–280.
- (60) Tamura, S. I.; Tanaka, Y.; Maris, H. J. Phonon group velocity and thermal conduction in superlattices. *Phys. Rev. B* **1999**, *60* (4), 2627–2630.
- (61) Berber, S.; Kwon, Y. K.; Tomanek, D. Unusually high thermal conductivity of carbon nanotubes. *Phys. Rev. Lett.* **2000**, *84*, 4613–4616.
- (62) Assael, M. J.; Metaxa, I. N.; Arvanitidis, J.; Christofilos, D.; Lioutas, C. Thermal conductivity enhancement in aqueous suspensions of carbon multi-walled and double-walled nanotubes in the presence of two different dispersants. *Int. J. Thermophys.* **2005**, *26*, 647–664.
- (63) Ward, C. A.; Neumann, A. W. On the surface thermodynamics of a two-component liquid–vapor–ideal solid system. *J. Colloid Interface Sci.* **1974**, *49* (2), 286–290.
- (64) Li, D.; Neumann, A. W. A reformulation of the equation of state for interfacial tensions. *J. Colloid Interface Sci.* **1990**, *137* (1), 304–307.
- (65) Spirk, S.; Ehmann, H. M.; Kargl, R.; Hurkes, N.; Reischl, M.; Novak, J.; Resel, R.; Wu, M.; Pietschnig, R.; Ribitsch, V. Surface modifications using a water-stable silanetriol in neutral aqueous media. *ACS Appl. Mater. Interfaces* **2010**, *2* (10), 2956–2962.
- (66) Pashley, R. M.; Israelachvili, J. N. A comparison of surface forces and interfacial properties of mica in purified surfactant solutions. *Colloids Surf.* **1981**, *2*, 169–187.
- (67) Vladkov, M.; Barrat, J.-L. Modeling transient absorption and thermal conductivity in a simple nanofluid. *Nano Lett.* **2006**, *6*, 1224–1228.
- (68) Musselman, S. W.; Chander, S. Wetting and adsorption of acetylenic diol based nonionic surfactants on heterogeneous surfaces. *Colloids Surf. A* **2002**, *206*, 497–513.
- (69) Every, A. G.; Tzou, Y.; Hasselman, D. P. H.; Raj, R. The effect of particle size on the thermal conductivity of ZnS/diamond composites. *Acta Metall. Mater.* **1992**, *40*, 123–129.
- (70) Reiss-Husson, F.; Luzzati, V. The structure of the micellar solutions of some amphiphilic compounds in pure water as determined by absolute small-angle X-ray scattering techniques. *J. Phys. Chem.* **1964**, *68* (12), 3504–3511.
- (71) Aswal, V. K.; Goyal, P. S. Counterions in the growth of ionic micelles in aqueous electrolyte solutions: A small-angle neutron scattering study. *Phys. Rev. E* **2000**, *61*, 2947–2953.
- (72) Hassan, P. A.; Yakhmi, J. V. Growth of cationic micelles in the presence of organic additives. *Langmuir* **2000**, *16*, 7187–7191.
- (73) Einstein, A. *Investigation on the Theory of the Brownian Motion*; Dover: New York, 1956.
- (74) Batchelor, G. K. The effect of Brownian motion on the bulk stress in a suspension of spherical particles. *J. Fluid Mech.* **1977**, *83*, 97–117.
- (75) Krieger, I. M.; Dougherty, T. J. A mechanism for non-Newtonian flow in suspensions of rigid spheres. *Trans. Soc. Rheol.* **1959**, *III*, 137–152.
- (76) Murshed, S. M. S.; Leong, K. C.; Yang, C. Enhanced thermal conductivity of TiO_2 –water based nanofluids. *Int. J. Therm. Sci.* **2005**, *44*, 367–373.
- (77) Philip, J.; Shima, P. D. Thermal properties of nanofluids. *Adv. Colloid Interface Sci.* **2012**, *183–184*, 30–45.